Plasmonic crystal defect nanolaser

Amit M. Lakhani, Myung-ki Kim, Erwin K. Lau, and Ming C. Wu*

Department of Electrical Engineering and Computer Sciences, University of California, Berkeley, CA 94720, USA
**wu@eecs.berkeley.edu*

Abstract: Surface plasmons are widely interesting due to their ability to probe nanoscale dimensions. To create coherent plasmons, we demonstrate a nanolaser based on a plasmonic bandgap defect state inside a surface plasmonic crystal. A one-dimensional semiconductor-based plasmonic crystal is engineered to have stopbands in which surface plasmons are prohibited from travelling in the crystalline structure. We then confine surface plasmons using a three-hole defect in the periodic structure. Using conventional III-V semiconductors, we achieve lasing in mode volumes as small as $V_{eff} = 0.3(\lambda_0/n)^3$ at $\lambda_0 = 1342$ nm, which is 10 times smaller than similar modes in photonic crystals of the same size. This demonstration should pave the way for achieving engineered nanolasers with deep-subwavelength mode volumes and attractive nanophotonics integration capabilities while enabling the use of plasmonic crystals as an attractive platform for designing plasmons.

OCIS codes: (140.5960) Semiconductor lasers; (350.4238) Nanophotonics and photonic crystals; (240.6680) Surface plasmons.

References and links

1. N. Fang, H. Lee, C. Sun, and X. Zhang, "Sub-diffraction-limited optical imaging with a silver superlens," Science **308**(5721), 534–537 (2005).
2. W. A. Challener, C. Peng, A. V. Itagi, D. Karns, W. Peng, Y. Peng, X. M. Yang, X. Zhu, N. J. Gokemeijer, Y. T. Hsia, G. Ju, R. E. Rottmayer, M. A. Seigler, and E. C. Gage, "Heat-assisted magnetic recording by a near-field transducer with efficient optical energy transfer," Nat. Photonics **3**(4), 220–224 (2009).
3. P. Alivisatos, "The use of nanocrystals in biological detection," Nat. Biotechnol. **22**(1), 47–52 (2004).
4. H. J. Lezec, J. A. Dionne, and H. A. Atwater, "Negative refraction at visible frequencies," Science **316**(5823), 430–432 (2007).
5. A. Artar, A. A. Yanik, and H. Altug, "Fabry–Pérot nanocavities in multilayered plasmonic crystals for enhanced biosensing," Appl. Phys. Lett. **95**(5), 051105 (2009).
6. D. Miller, "Device requirements for optical interconnects to silicon chips," Proc. IEEE **97**(7), 1166–1185 (2009).
7. J. A. Dionne, L. A. Sweatlock, M. T. Sheldon, A. P. Alivisatos, and H. A. Atwater, "Silicon-based plasmonics for on-chip photonics," IEEE J. Sel. Top. Quantum Electron. **16**(1), 295–306 (2010).
8. R. F. Oulton, V. J. Sorger, D. A. Genov, D. F. P. Pile, and X. Zhang, "A hybrid plasmonic waveguide for subwavelength confinement and long-range propagation," Nat. Photonics **2**(8), 496–500 (2008).
9. H. T. Miyazaki and Y. Kurokawa, "Controlled plasmon resonance in closed metal/insulator/metal nanocavities," Appl. Phys. Lett. **89**(21), 211126 (2006).
10. V. J. Sorger, R. F. Oulton, J. Yao, G. Bartal, and X. Zhang, "Plasmonic Fabry-Pérot nanocavity," Nano Lett. **9**(10), 3489–3493 (2009).
11. S. I. Bozhevolnyi, V. S. Volkov, E. Devaux, J.-Y. Laluet, and T. W. Ebbesen, "Channel plasmon subwavelength waveguide components including interferometers and ring resonators," Nature **440**(7083), 508–511 (2006).
12. D. F. P. Pile and D. K. Gramotnev, "Adiabatic and nonadiabatic nanofocusing of plasmons by tapered gap plasmon waveguides," Appl. Phys. Lett. **89**(4), 041111 (2006).
13. S. Vedantam, H. Lee, J. Tang, J. Conway, M. Staffaroni, and E. Yablonovitch, "A plasmonic dimple lens for nanoscale focusing of light," Nano Lett. **9**(10), 3447–3452 (2009).
14. M. T. Hill, Y.-S. Oei, B. Smalbrugge, Y. Zhu, T. de Vries, P. J. van Veldhoven, F. W. M. van Otten, T. J. Eijkemans, J. P. Turkiewicz, H. de Waardt, E. J. Geluk, S.-H. Kwon, Y.-H. Lee, R. Notzel, and M. K. Smit, "Lasing in metallic-coated nanocavities," Nat. Photonics **1**(10), 589–594 (2007).
15. M. T. Hill, M. Marell, E. S. P. Leong, B. Smalbrugge, Y. Zhu, M. Sun, P. J. van Veldhoven, E. J. Geluk, F. Karouta, Y.-S. Oei, R. Nötzel, C.-Z. Ning, and M. K. Smit, "Lasing in metal-insulator-metal sub-wavelength plasmonic waveguides," Opt. Express **17**(13), 11107–11112 (2009).
16. M. A. Noginov, G. Zhu, A. M. Belgrave, R. Bakker, V. M. Shalaev, E. E. Narimanov, S. Stout, E. Herz, T. Suteewong, and U. Wiesner, "Demonstration of a spaser-based nanolaser," Nature **460**(7259), 1110–1112 (2009).

#151200 - $15.00 USD Received 19 Jul 2011; revised 13 Aug 2011; accepted 13 Aug 2011; published 1 Sep 2011

17. R. F. Oulton, V. J. Sorger, T. Zentgraf, R.-M. Ma, C. Gladden, L. Dai, G. Bartal, and X. Zhang, "Plasmon lasers at deep subwavelength scale," Nature **461**(7264), 629–632 (2009).
18. K. Yu, A. Lakhani, and M. C. Wu, "Subwavelength metal-optic semiconductor nanopatch lasers," Opt. Express **18**(9), 8790–8799 (2010).
19. M. P. Nezhad, A. Simic, O. Bondarenko, B. Slutsky, A. Mizrahi, L. Feng, V. Lomakin, and Y. Fainman, "Room-temperature subwavelength metallo-dielectric lasers," Nat. Photonics **4**(6), 395–399 (2010).
20. C.-Y. Lu, S.-W. Chang, S. L. Chuang, T. D. Germann, and D. Bimberg, "Metal-cavity surface-emitting microlaser at room temperature," Appl. Phys. Lett. **96**(25), 251101 (2010).
21. S.-H. Kwon, J.-H. Kang, C. Seassal, S.-K. Kim, P. Regreny, Y.-H. Lee, C. M. Lieber, and H.-G. Park, "Subwavelength plasmonic lasing from a semiconductor nanodisk with silver nanopan cavity," Nano Lett. **10**(9), 3679–3683 (2010).
22. A. M. Lakhani, K. Yu, and M. C. Wu, "Lasing in subwavelength semiconductor nanopatches," Semicond. Sci. Technol. **26**(1), 014013 (2011).
23. R.-M. Ma, R. F. Oulton, V. J. Sorger, G. Bartal, and X. Zhang, "Room-temperature sub-diffraction-limited plasmon laser by total internal reflection," Nat. Mater. **10**(2), 110–113 (2011).
24. K. Ding, Z. Liu, L. Yin, H. Wang, R. Liu, M. T. Hill, M. J. H. Marell, P. J. van Veldhoven, R. Nötzel, and C. Z. Ning, "Electrical injection, continuous wave operation of subwavelength-metallic-cavity lasers at 260 K," Appl. Phys. Lett. **98**(23), 231108 (2011).
25. S. L. McCall, A. F. J. Levi, R. E. Slusher, S. J. Pearton, and R. A. Logan, "Whispering-gallery mode microdisk lasers," Appl. Phys. Lett. **60**(3), 289 (1992).
26. J. C. Johnson, H.-J. Choi, K. P. Knutsen, R. D. Schaller, P. Yang, and R. J. Saykally, "Single gallium nitride nanowire lasers," Nat. Mater. **1**(2), 106–110 (2002).
27. Z. Zhang, L. Yang, V. Liu, T. Hong, K. Vahala, and A. Scherer, "Visible submicron microdisk lasers," Appl. Phys. Lett. **90**(11), 111119 (2007).
28. S. Reitzenstein, T. Heindel, C. Kistner, A. Rahimi-Iman, C. Schneider, S. Hofling, and A. Forchel, "Low threshold electrically pumped quantum dot-micropillar lasers," Appl. Phys. Lett. **93**(6), 061104 (2008).
29. M.-K. Kim, S. H. Lee, M. Choi, B.-H. Ahn, N. Park, Y.-H. Lee, and B. Min, "Low-loss surface-plasmonic nanobeam cavities," Opt. Express **18**(11), 11089–11096 (2010).
30. O. Painter, R. K. Lee, A. Scherer, A. Yariv, J. D. O'Brien, P. D. Dapkus, and I. Kim, "Two-dimensional photonic band-Gap defect mode laser," Science **284**(5421), 1819–1821 (1999).
31. H.-G. Park, S.-H. Kim, S.-H. Kwon, Y.-G. Ju, J.-K. Yang, J.-H. Baek, S.-B. Kim, and Y.-H. Lee, "Electrically driven single-cell photonic crystal laser," Science **305**(5689), 1444–1447 (2004).
32. H. Matsubara, S. Yoshimoto, H. Saito, Y. Jianglin, Y. Tanaka, and S. Noda, "GaN photonic-crystal surface-emitting laser at blue-violet wavelengths," Science **319**(5862), 445–447 (2008).
33. Y. Kurosaka, S. Iwahashi, Y. Liang, K. Sakai, E. Miyai, W. Kunishi, D. Ohnishi, and S. Noda, "On-chip beam-steering photonic-crystal lasers," Nat. Photonics **4**(7), 447–450 (2010).
34. Y. Gong, B. Ellis, G. Shambat, T. Sarmiento, J. S. Harris, and J. Vuckovic, "Nanobeam photonic crystal cavity quantum dot laser," Opt. Express **18**(9), 8781–8789 (2010).
35. T. Okamoto, F. H'Dhili, and S. Kawata, "Towards plasmonic band gap laser," Appl. Phys. Lett. **85**(18), 3968 (2004).
36. E. K. Lau, A. Lakhani, R. S. Tucker, and M. C. Wu, "Enhanced modulation bandwidth of nanocavity light emitting devices," Opt. Express **17**(10), 7790–7799 (2009).
37. C. Jeppesen, N. A. Mortensen, and A. Kristensen, "The effect of Ti and ITO adhesion layers on gold split-ring resonators," Appl. Phys. Lett. **97**(26), 263103 (2010).

1. Introduction

Nanophotonic circuits/devices using metal-optics/surface plasmons uniquely manipulate light below the diffraction limit, enabling countless applications including imaging [1], data storage [2], optical sensing [3–5], and optical interconnection [6,7]. Passive plasmonic structures such as waveguides [7,8], resonators [9,10], and interferometers [11] have been demonstrated. Nanolasers with the ability to easily couple into nanophotonic circuits have become critical to realize nanoscale optics since external lasers suffer from low coupling efficiency [2] even with designed couplers [12,13]. Recently, several nanolasers have been reported using varying degrees of dielectric and metallic confinement to achieve subwavelength mode volumes [14–24], shrinking lasers beyond traditional dielectric cavities [25–28]. Among these, surface-plasmon-based nanolasers [16,17,21,23] have been demonstrated as enablers to plasmonic circuits. Yet, easy design of nanophotonic circuits will only be possible with a unifying platform where active and passive components can exist simultaneously.

Recently, Kim et al. have theorized that combining concepts from photonic crystal structures with plasmonics can be a powerful way to engineer coupled subwavelength light sources with passive components [29]. In conventional photonic crystal lasers [30,31], the mode patterns and coupling schemes of lasers are easily engineered by designing the size and location of the air holes [32,33]. However, the laser mode is limited by the diffraction limit

#151200 - $15.00 USD Received 19 Jul 2011; revised 13 Aug 2011; accepted 13 Aug 2011; published 1 Sep 2011

[30,34]. To overcome this hurdle, we demonstrate a nanolaser based on a defect inside a surface plasmon polariton crystal (SPPC or plasmonic crystal). A SPPC is simply a periodic structure on a metal film capable of manipulating surface plasmons at the metal/dielectric interface. It is engineered to have stopbands that inhibit travelling surface plasmons of certain frequencies. Recent attempts at creating such devices have not been able to overcome resistive losses [35]. In this paper, we experimentally localize plasmon oscillations using a defect in this periodic structure and achieve lasing in mode volumes of $V_{eff} = 0.3\ (\lambda_0/n)^3$ at $\lambda_0 = 1342$ nm for the first time. We envision that plasmonic crystals will be useful for not only nanolasers, but also Purcell-enhanced light-emitting diodes capable of modulation speeds >100GHz due to the exquisite controllability of electromagnetic mode volumes [36]. With this nanolaser demonstration, we enable plasmonic crystals to become a new paradigm for the development of robust and engineered active nanophotonic circuits capable of incorporating deep-subwavelength light emitters.

2. Device geometry and fabrication

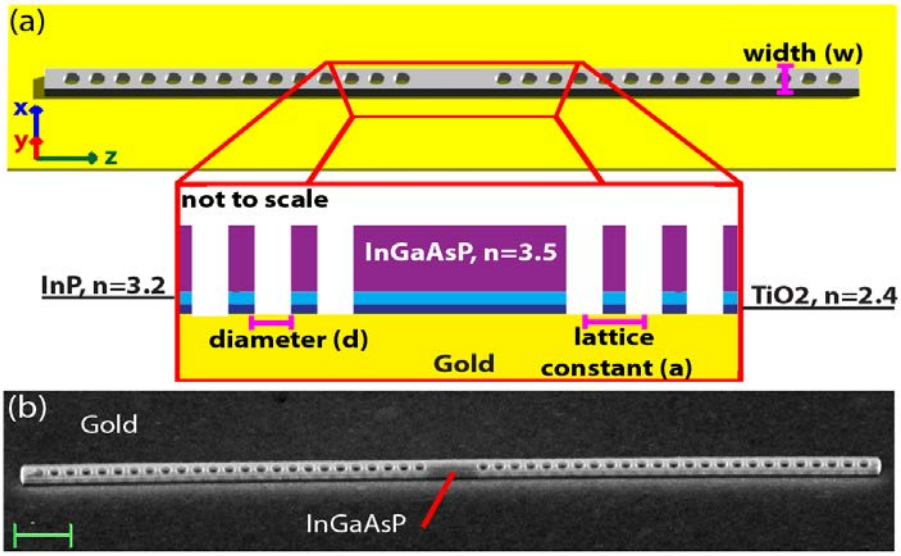

Fig. 1. (a) A schematic of a one-dimensional plasmonic crystal. The nanobeam consists of a direct-gap semiconductor material (InGaAsP) with a 5 nm TiO2 dielectric barrier and a 10 nm InP barrier between it and the metal. The 3 nm Ti adhesion layer is left off for simplicity. The device has three air holes missing in the middle of the device, creating a defect in the periodic structure. The beam is 225 nm thick and *w* wide with air holes of diameter *d* spaced apart by lattice constant *a*. (b) A scanning electron micrograph of a one-dimensional plasmonic crystal. The scale bar represents 1 μm.

In Fig. 1a, we show the geometry of the plasmonic crystal defect nanolaser. A periodically patterned nanobeam of InGaAsP/InP is placed on a 100-nm thick gold film with a 3nm Ti adhesion layer and a 5 nm TiO2 spacer layer. The device has three air holes missing in the center and has a width *w*, lattice constant *a*, and hole diameter *d*. The nanobeam consists of a 200-nm InGaAsP layer sandwiched by 10 nm of InP barrier material. The metal underneath the semiconductor is as smooth as the initial semiconductor surface due to the nature of the fabrication process. However, after RIE etching, the metal surface surrounding the device is roughened, although the exact average roughness was not measured. A fabricated device can be seen in Fig. 1b. Details of the fabrication process are described elsewhere [18].

3. Properties of plasmonic crystals

A plasmonic crystal is heavily influenced by the presence of the metal film compared to a photonic crystal structure surrounded completely by air of the same size. In Fig. 2, we contrast

#151200 - $15.00 USD Received 19 Jul 2011; revised 13 Aug 2011; accepted 13 Aug 2011; published 1 Sep 2011

various aspects of plasmonic and photonic crystals. In Fig. 2a and 2b, we show the simulated dispersion of the device shown in Fig. 6a below with and without a metal film, respectively. The crystal dispersion was generated using finite difference time domain (FDTD) techniques with periodic boundary conditions. In a photonic crystal, the TM modes operate at much higher frequency relative to the SPPC and do not form a bandgap (e.g. A' and B' are nearly degenerate at the Brillouin zone edge). The dielectric structure does, however, have a bandgap for TE travelling waves. In contrast, in a plasmonic crystal, the TM travelling waves present in the photonic crystal interact heavily with the metal film and become surface plasmons (Fig. 3). As a result, their operating frequencies drop (e.g. band A' is at 280 THz while band A is at 190 THz at the band-edge), and, more importantly, the metal film interaction separates the photonic TM modes at the crystal band-edge and allows for the creation of defects that can successfully confine plasmons in a SPPC. These pseudo-bandgaps appear at the edge of the Brillouin zone between bands A and B and also between bands C and D (Fig. 2a). Finally, the metal film breaks the symmetry of the photonic crystal in the y-direction, causing the non-interacting photonic modes to blue shift.

Using the absence of three holes in the middle of the crystal, multiple defect modes can be created. Because of the large difference between the two devices, the fundamental defect modes (α and α') for both structures in Fig. 4 also have different characteristics. The α' mode resonates at 235THz and is TE, while α resonates at 193 THz and is TM; the photonic crystal would have to be roughly ~1.25 times larger to match the plasmonic crystal resonance

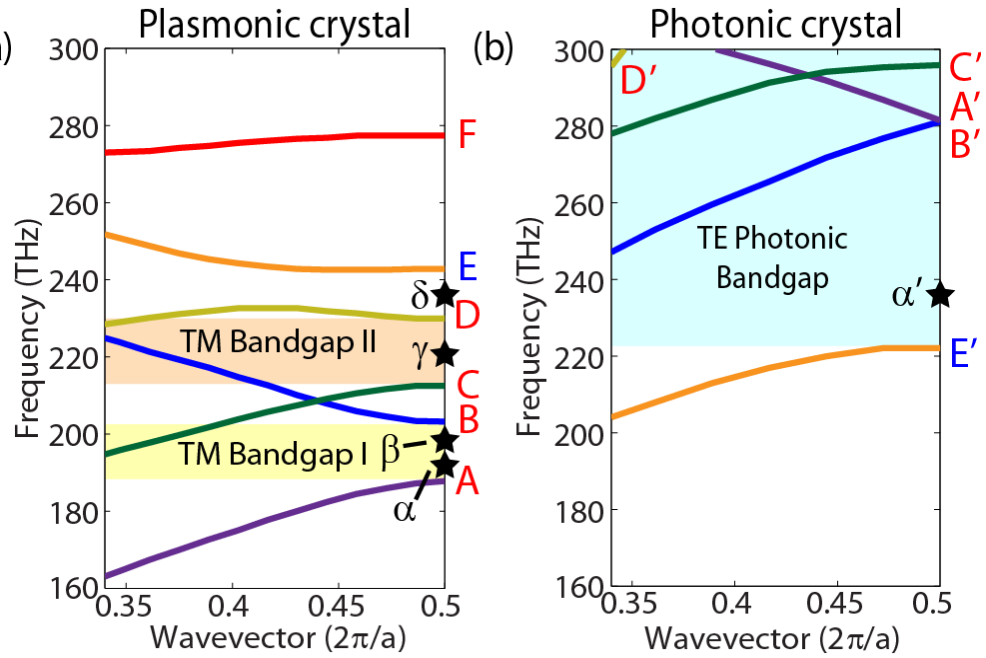

Fig. 2. We contrast the plasmonic crystal with a photonic crystal of the same dimensions. (a) The simulated band structure for the plasmonic crystal device in Fig. 3a. We show the first six bands of the device (A-F). The bands are labeled red (TM/plasmonic) and blue (TE/photonic). We also highlight the presence of two plasmonic bandgaps that appear only in the plasmonic crystal (versus a photonic crystal). A three hole defect in the device introduces multiple defect eigenmodes shown as black stars at the Broullion zone edge. (b) We show the simulated band structure for a photonic crystal with exact dimensions in Fig. 3a but *without* the metal substrate. The bands are labeled to correspond to a particular travelling wave of a plasmonic crystal (e.g. A' in a photonic crystal corresponds with A in the plasmonic crystal). The photonic crystal has only a TE bandgap that extends from 222 THz to beyond 300 THz with a defect mode, α' due to a three hole defect.

#151200 - $15.00 USD Received 19 Jul 2011; revised 13 Aug 2011; accepted 13 Aug 2011; published 1 Sep 2011

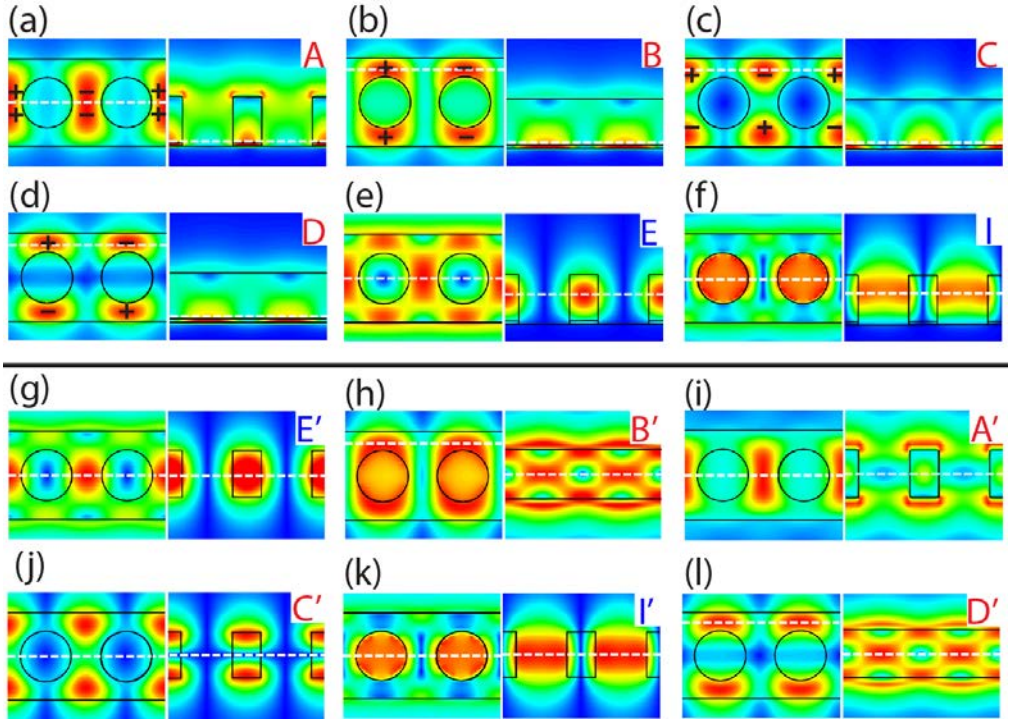

Fig. 3. We contrast the different bands for a plasmonic and photonic crystal of the same dimensions. The bands are labeled to correspond to Fig. 1. (a, b, c, d, e, f) The electric field magnitude plots of the first four plasmonic bands (A-D) and the first two photonic bands (E,I) are presented for a SPPC. The charge distribution of the plasmon-like (TM) bands (A-D) are overlaid on the field distribution plots. Each pair of plots correspond to a color map of $|E|$ along the cross-section defined by the dashed white line on the corresponding figure. The left plot is in the x-z plane, while the right figure is in the y-z plane. Bands A, B, C, D, E, and I resonate at 190, 204, 214, 229, 243, and 327 THz, respectively. (g, h, i, j, k, l) In a similar manner, we show the electric field magnitude plots of the first six bands for a photonic crystal in order of increasing resonance frequency (E', B', A', C', I', and D' resonate at 222, 282, 283, 295, 310, and 312 THz, respectively).

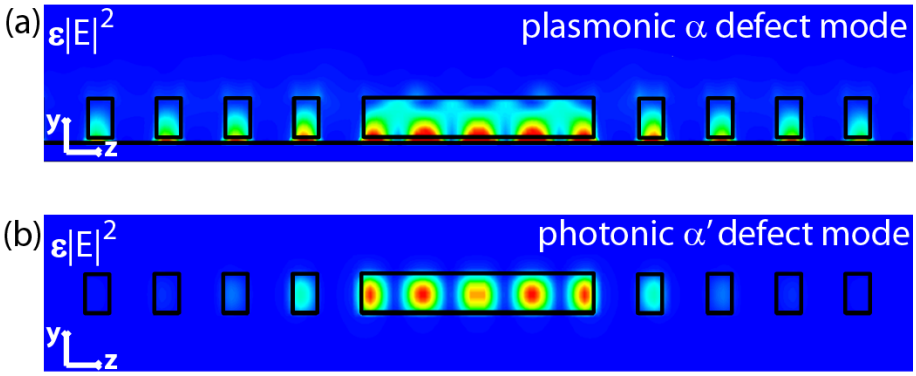

Fig. 4. (a) A profile in the y-z plane of the electric energy density of the α defect mode in a plasmonic crystal with metal beneath the semiconductor beam. The defect mode is TM/plasmonic in nature. (b) Another profile in the y-z plane of the electric energy density of the α' defect mode of the photonic crystal. This mode is TE/photonic in nature in contrast to the α defect mode

frequency (more size reduction is expected in visible frequencies due to the nature of surface plasmon wavevectors). We define the electromagnetic mode volume of the lasing mode as V_{eff}

#151200 - $15.00 USD Received 19 Jul 2011; revised 13 Aug 2011; accepted 13 Aug 2011; published 1 Sep 2011

$= \int(\partial(\omega\varepsilon(\boldsymbol{r},\omega))/\partial\omega)|\boldsymbol{E}(\boldsymbol{r})|^2 d^3\boldsymbol{r}/max((\partial(\omega\varepsilon(\boldsymbol{r},\omega))/\partial\omega)|\boldsymbol{E}(\boldsymbol{r})|^2)$ so that the photonic crystal defect has $V_{eff,\alpha'} = 0.6\ (\lambda_0/n)^3$ while the plasmonic defect mode has a volume of $V_{eff,\alpha} = 0.1\ (\lambda_0/n)^3$. The maximum energy point was found to be in the semiconductor for the α mode. Thus, the plasmonic α defect mode volume is 6 times smaller than the photonic counterpart.

4. Plasmonic crystal defect modes

In the SPPC, we observe lasing with the γ and δ defect modes. The α and β defect modes are not experimentally observed in this study probably due to insufficient gain with the current material system and the use of titanium as an adhesion layer between the gold and semiconductor interface [37]. In the future, low-loss metals and high-gain semiconductors will elucidate these modes. We show a summary of different relevant laser parameters for the first four defect modes of a 3-hole cavity in a plasmonic crystal in Fig. 5a. We also show the mode profiles for the α and β defect modes in Figs. 5b and 5c, respectively.

(a)

	α	β	γ	δ
Q_{total}	71	73	90	143
$Q_{radiation}$	308	438	2380	3550
Q_{loss}	92	88	94	149
$V_{effective}/(\lambda/n)^3$	0.1	0.15	0.3	0.7
Confinement Factor	67%	62%	63%	76%

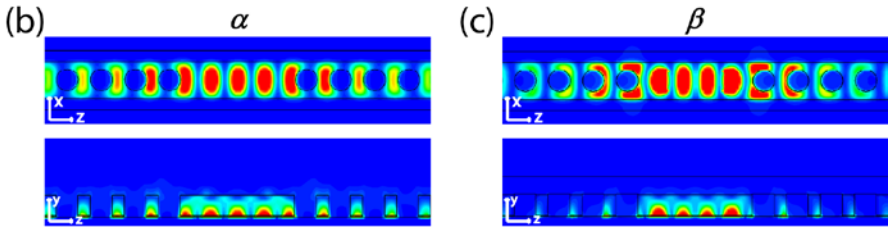

Fig. 5. (a) Summary table of relevant laser parameters of the first four eigenmodes of a 3-hole defect in a one-dimensional plasmonic crystal. (b,c) The top and side profiles of the electric energy density of the α and β defect modes. Both modes are surface plasmon modes that decay evanescently from the gold/semiconductor interface.

The γ mode's eigenfrequency is in the second pseudo-bandgap between bands C and D. The presence of the C and D bands and the γ defect mode was experimentally verified in Figs. 7a and 7b below. Although the second bandgap is not truly forbidden (due to Band B), the third defect mode does not couple well to the band because the modes have opposite parity along the y-z plane. A scanning electron micrograph (SEM) of a device where the γ mode lases dominantly is seen in Fig. 6a. The γ defect mode is purely a surface plasmon mode, with evanescent decay in both the metal and semiconductor (Figs. 6b and 6c). The modal volume of the simulated structure is $V_{eff} = 0.30\ (\lambda_0/n)^3$, where $n = 3.5$ is the index of InGaAsP. The third photonic defect mode (γ') has a mode volume of ~3 $(\lambda_0/n)^3$ (λ_0 is 970nm), making the plasmonic crystal defect 10 times smaller in electromagnetic mode volume. The mode is also confined in the semiconductor so that ~66% of the mode's energy resides in the gain media, where the electric energy density is defined as $U = \int(\partial(\omega\varepsilon)/\partial\omega)|\boldsymbol{E}(\boldsymbol{r})|^2 d^3\boldsymbol{r}$. This defect mode has a cold-cavity quality factor at room temperature of $Q_{Ag} = 330$ if silver is used with no Ti adhesion layer, $Q_{Au} = 90$ if gold is used without a titanium adhesion layer, and $Q_{mode3} = 33$ if gold is used with a 3nm titanium adhesion layer (assuming bulk titanium properties). With the current design, the radiation quality factor is $Q_{rad} = 2380$. In our fabrication, we use Ti/Au even though the quality factor of the cavity is lower due to ease of fabrication. Finally, δ resonates at energies larger than modes in the D band (Fig. 2a).

#151200 - $15.00 USD Received 19 Jul 2011; revised 13 Aug 2011; accepted 13 Aug 2011; published 1 Sep 2011

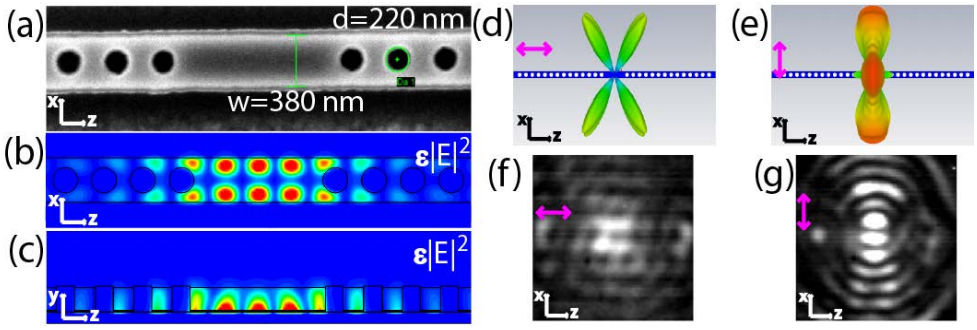

Fig. 6. We observe lasing in the γ defect mode of a SPPC and show the electromagnetic properties of a γ-defect nanolaser. (a) SEM micrograph of a device in which the γ defect mode lases. It has a lattice constant of a = 343 nm. (b,c) The top (x-z) view and the side (y-z) view of the electric energy density of the γ defect resonance (d,e) The simulated z-polarized and x-polarized far-field radiation directivity of the γ defect mode. The device is shown for reference. (f,g) Experimentally obtained z-polarized and x-polarized images of the γ lasing mode.

5. Experimental results

The plasmonic crystal defect lasers were studied using pulsed optical pumping at 77 Kelvin. Details of the measurement setup are found elsewhere [18]. Out of the many working devices that were fabricated, we have chosen one to illustrate lasing from the γ defect mode (Fig. 6a). Taking geometrical measurements from SEM, the device was simulated using Finite Integral technique (FIT) and the computed eigenfrequencies of various resonances agreed well with experimental data (Fig. 7). Using micro-photoluminescence, we verify that the band edge modes appear brightest when the edge of the device is optically pumped, whereas the defect mode only lases when the center of the device is pumped. In almost all instances, lasing is seen from band edge modes as well (Fig. 8). To further verify that the γ mode was lasing, we imaged the radiation from the device ~5 μm above the sample plane under maximum pumping conditions using a 100X 0.8NA objective (Figs. 6f and 6g). These polarization-resolved patterns were compared to simulated far-field radiation directivity of the γ defect mode (Figs. 6d and 6e). There is strong qualitative correspondence between the measured and simulated patterns. Also, in simulation and experiment, the z-polarized light was 10 and 8 times weaker than the x-polarized light, respectively.

The lasing spectrum at maximum pumping power of the plasmonic crystal defect laser can be seen in Fig. 7c. The threshold pumping power was found to be ~100 kW/cm^2. However, this threshold is artificially high, since not all the pump power was absorbed by the structure due to its size. The linewidth of the laser was found to be to 0.5 nm at maximum pumping power. The peak wavelength of the device also stabilizes as lasing is reached, since carrier dependent refractive index changes are stabilized due to carrier clamping. We also analyzed the pump-power-dependent light output (L-L curve) for the γ defect mode. The integrated intensity from the defect cavity mode is seen in Fig. 7d. The spontaneous emission rate is enhanced in the nanocavity due to high coupling of spontaneous emission into the laser mode (β) and the Purcell effect ($F = (16/\pi^2)(Q/V_{eff})(\lambda/n)^3$). The light output characteristics of the nanolaser (L-L curve) were analyzed using rate equations and previously published material parameters [18]. Taking into account the above effects regarding spontaneous emission, a good fit of the experimental data was obtained using a rate equation model with a fitting parameter $F\beta$ = 0.122 (Fig. 7d).

In order to calculate a realistic Purcell enhancement, an experimentally determined quality factor for each mode needs to be measured. However, because of loss and gain within the semiconductor material, an accurate measurement of quality factors is difficult. The quality factor of plasmonic crystal lasers is metal-loss dominated, and thus should improve at low temperatures. The lowest measured quality factor for the γ mode was Q_{meas} = 250. Yet, this quality factor probably does not represent the actual nature of the defect cavity. Thus, in

#151200 - $15.00 USD Received 19 Jul 2011; revised 13 Aug 2011; accepted 13 Aug 2011; published 1 Sep 2011

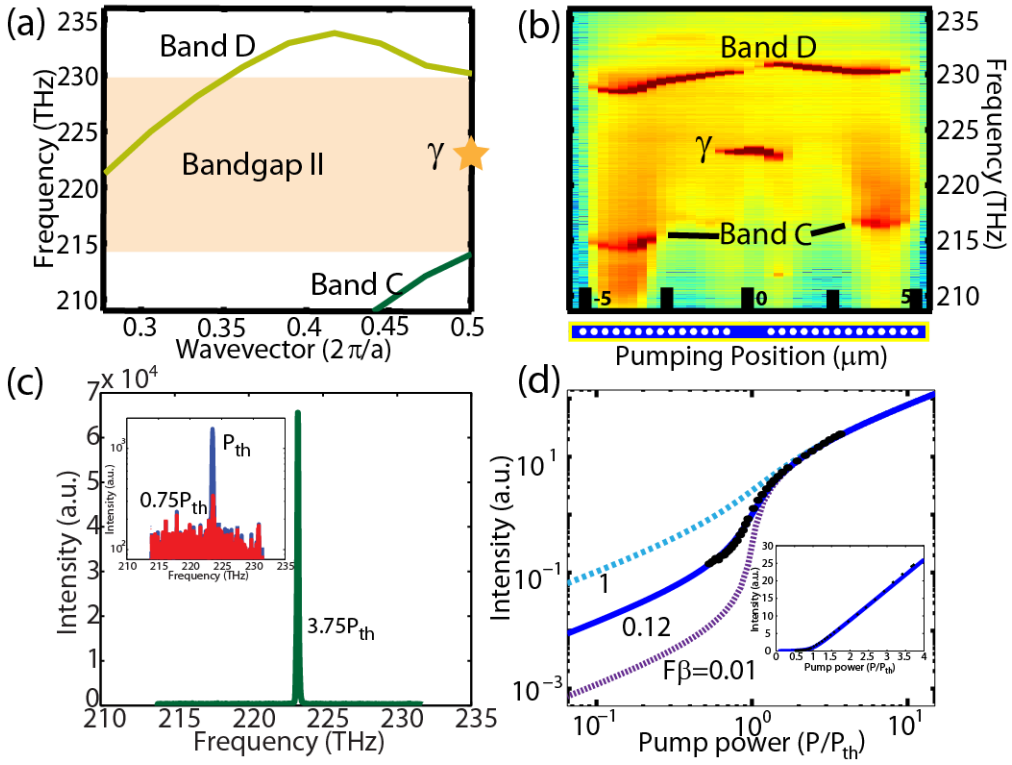

Fig. 7. Laser characteristics of the γ defect laser mode. (a) The simulated plasmonic dispersion, bandgap, and defect location of the device in Fig. 3a. The γ defect has a resonance frequency near 224 THz. (b) The spectra obtained from the device shown in Fig. 3a versus pump position along the device (the spot size is ~3 μm). Away from the center of the device, bands C and D are observed and confirmed through agreement with simulation in (a). The third defect begins to lase when the device is pumped in the device center (where the defect is located). (c) The lasing spectra of the γ defect mode. The inset shows the laser spectrum in semi-log scale below and at threshold pump power. (d) The input-output power characteristics (L-L curve) of the γ defect in log-log scale. Using rate equation models, it is estimated that the device has large spontaneous emission coupling into the laser mode with Fβ = 0.122. L-L curves with Fβ = 0.01 and Fβ = 1 are shown for comparison to the obtained data (black circles). Also, the L-L curve is plotted in linear scale (inset).

fitting the $F\beta$ product for each L-L curve, we used a range of values for quality factors of the cavity, keeping in mind that previously published results suggest that metal loss is decreased by 5 times at 77K relative to room temperature [14]. There is also uncertainty in the mode volume used in the Purcell factor calculation, since not every carrier recombines that the point of maximum energy density. We suggest that quality factors near 5 times the simulated quality factors (including Ti loss) are most accurate (Q_{model} = 180), and the simulated mode volumes is also accurate (V_{eff} = 0.30 $(\lambda_0/n)^3$) giving F = 15.33. Yet, even if we vary F = 1.5 – F = 21, the product $F\beta$ changes only modestly from $F\beta$ = 0.090-0.126, suggesting that a relatively good model for spontaneous emission can be ascertained even with uncertainty in cavity quality factors and mode volumes.

We also observed lasing from the plasmonic travelling waves inside the SPPC. At the edge of the Broullion zone of the plasmonic crystal, the group velocities of the travelling modes go to zero. Thus, very large gain can be achieved for bandedge modes in plasmonic crystal cavities. In Fig. 8, the lasing characteristics of band D are shown in a different device than in Fig. 6a but with very similar dimensions. The band edge mode can selectively lase when the device is pumped at the edge (away from the defect area). Band C is suppressed because it is not in the gain bandwidth in this particular device. In band D, the group velocity approaches

#151200 - $15.00 USD Received 19 Jul 2011; revised 13 Aug 2011; accepted 13 Aug 2011; published 1 Sep 2011

zero at the band edge and at k~0.42 (2π/a) (Fig. 2a). Lasing in a plasmonic band mode seems to behave very classically with a sharp threshold, as seen in the pump vs. intensity characteristics of the representative device in Fig. 8c. Although we cannot know the mode volume and theoretical quality factor of the band mode laser, we estimate the product $F\beta$ = 0.016 from simple fitting by rate equation analysis. Thus, the spontaneous emission coupling is greatly reduced relative to a localized defect mode seen in Fig. 7.

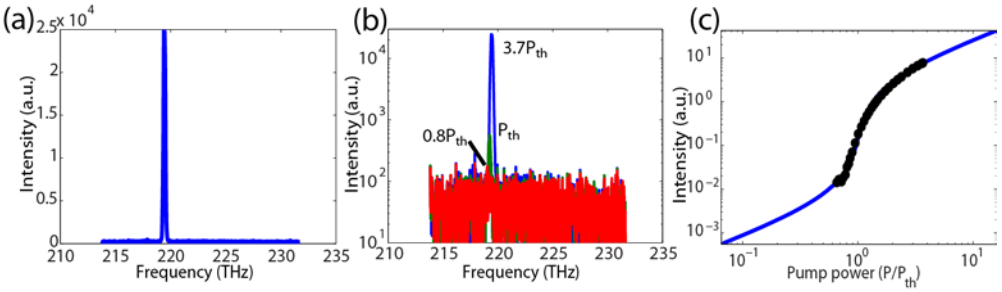

Fig. 8. We show laser characteristics from band D. (a) We show a lasing spectrum obtained at a peak pump power of 380 kW/cm2. (b) The semi-log scale pump-dependent spectra for the band-mode. (c) The L-L curve shows that the bandedge mode has a sharper threshold than the γ defect mode. The threshold pump power for this device is 55kW/cm2 of peak power.

6. Discussion and Conclusion

This particular demonstration of a SPPC-based nanolaser highlights only the beginning of this technology's potential. In the future, plasmonic crystals, like their photonic counterparts, should be able to confine plasmons to one-half of a wavelength ($\lambda_{sp}/2$) .Thus, single-sided SPPCs should be able to squeeze electromagnetic mode volumes to less than 0.01 $(\lambda_0/n)^3$ at visible frequencies, where n = 3.5 and the surface plasmon is propagating at a gold/semiconductor interface. In the near-infrared frequency range, using single-hole defects will further reduce the mode volume of our cavities. Utilizing better fabrication techniques without a lossy titanium layer should further allow our nanolaser to operate in the α mode, which is 3 times smaller in electromagnetic mode volume. Metal-semiconductor-metal geometries coupled with plasmonic crystals will also be able to squeeze mode volumes much below the limit of a single-sided surface plasmon at near-infrared frequencies [9,15]. Finally, SPPC's (especially metal-semiconductor-metal geometries) promise facile implementation of electrically-driven nano-emitters coupled to plasmonic waveguides since the metal can also serve as contacts [28].

In summary, we have successfully shown the operation of a plasmonic crystal defect laser within a plasmonic bandgap based upon semiconductor technology. This laser benefits from small mode volumes with $V_{eff} = 0.3(\lambda_0/n)^3$ at λ_0 = 1342 nm, making it 10 times smaller than a similar mode in a photonic crystal of the same physics dimensions. This initial demonstration of a nanolaser based on plasmonic crystals should enable to use of these structures to generate coherent plasmons and control them in great detail, making them suitable as a future nanophotonics platform. The integration of the nanolaser with a plasmonic crystal while maintaining ultra-small mode volumes makes a plasmonic crystal defect laser a strong contender as a coherent light source for nano-opto-electronics in the future and enables the use of plasmonic crystals as a tool for mode volume engineering for all nano-light-emitters.

Acknowledgments

The authors would like to thank Michael Eggleston, Ryan Going, and Tae Joon Seok for their helpful discussion. This material is based upon work supported under a National Science Foundation Graduate Research Fellowship. This project was also supported by DARPA NACHOS (W911NF-07-1-0314), the NSF Center for Integrated Access Networks (CIAN) (EEC-08120702), the NSF Center for Energy Efficient Electronics Science (E3S) (ECCS-0939514), and Samsung GRO (20101554).

#151200 - $15.00 USD Received 19 Jul 2011; revised 13 Aug 2011; accepted 13 Aug 2011; published 1 Sep 2011